doi:10.1093/brain/awr278 Brain 2011: 134; 3602–3615 | 3602

BRAIN
A JOURNAL OF NEUROLOGY

Tracking iron in multiple sclerosis: a combined imaging and histopathological study at 7 Tesla

Francesca Bagnato,[1,*] Simon Hametner,[2,*] Bing Yao,[3] Peter van Gelderen,[3] Hellmut Merkle,[3] Fredric K. Cantor,[4] Hans Lassmann[2] and Jeff H. Duyn[3]

1 National Institutes of Neurological Disorders and Stroke (NINDS), National Institutes of Health, Bethesda, MD, USA
2 Centre for Brain Research, Medical University, Vienna, Austria
3 Advanced Magnetic Resonance Imaging Section, Laboratory of Functional and Molecular Imaging, NINDS, NIH, Bethesda, MD, USA
4 Neuroimmunology Branch (NIB), NINDS, NIH, Bethesda, MD, USA

*These authors contributed equally to this work.

Correspondence to: F. Bagnato, MD, PhD
Department of Radiology and Radiological Sciences,
Institute of Imaging Science,
Vanderbilt University,
1161 21st Ave. S. AA1105 MCN
Nashville, TN 37232, USA
E-mail: francesca.r.bagnato@vanderbilt.edu

Previous authors have shown that the transverse relaxivity R_2* and frequency shifts that characterize gradient echo signal decay in magnetic resonance imaging are closely associated with the distribution of iron and myelin in the brain's white matter. In multiple sclerosis, iron accumulation in brain tissue may reflect a multiplicity of pathological processes. Hence, iron may have the unique potential to serve as an *in vivo* magnetic resonance imaging tracer of disease pathology. To investigate the ability of iron in tracking multiple sclerosis-induced pathology by magnetic resonance imaging, we performed qualitative histopathological analysis of white matter lesions and normal-appearing white matter regions with variable appearance on gradient echo magnetic resonance imaging at 7 Tesla. The samples used for this study derive from two patients with multiple sclerosis and one non-multiple sclerosis donor. Magnetic resonance images were acquired using a whole body 7 Tesla magnetic resonance imaging scanner equipped with a 24-channel receive-only array designed for tissue imaging. A 3D multi-gradient echo sequence was obtained and quantitative R_2* and phase maps were reconstructed. Immunohistochemical stainings for myelin and oligodendrocytes, microglia and macrophages, ferritin and ferritin light polypeptide were performed on 3- to 5-μm thick paraffin sections. Iron was detected with Perl's staining and 3,3′-diaminobenzidine-tetrahydrochloride enhanced Turnbull blue staining. In multiple sclerosis tissue, iron presence invariably matched with an increase in R_2*. Conversely, R_2* increase was not always associated with the presence of iron on histochemical staining. We interpret this finding as the effect of embedding, sectioning and staining procedures. These processes likely affected the histopathological analysis results but not the magnetic resonance imaging that was obtained before tissue manipulations. Several cellular sources of iron were identified. These sources included oligodendrocytes in normal-appearing white matter and activated macrophages/microglia at the edges of white matter lesions. Additionally, in white matter lesions, iron precipitation in aggregates typical of microbleeds was shown by the Perl's staining. Our combined imaging and pathological study shows that multi-gradient echo magnetic resonance imaging is a sensitive technique for the identification of iron in the brain tissue of patients with multiple sclerosis. However, magnetic resonance

Received May 21, 2011. Revised August 8, 2011. Accepted August 24, 2011

imaging-identified iron does not necessarily reflect pathology and may also be seen in apparently normal tissue. Iron identification by multi-gradient echo magnetic resonance imaging in diseased tissues can shed light on the pathological processes when coupled with topographical information and patient disease history.

Keywords: multiple sclerosis; iron; myelin; magnetic resonance imaging; multi-gradient echo magnetic resonance imaging

Abbreviations: DAB = 3,3′-diaminobenzidine-tetrahydrochloride; WML = white matter lesion

Introduction

Currently available MRI techniques are highly sensitive in detecting white matter lesions of patients with multiple sclerosis but lack pathological specificity. Identifying white matter lesion pathological specificity is rather crucial, as it could permit a better understanding of the mechanisms underlying the disease and patient disability. With the hope of improving characterization of white matter multiple sclerosis-induced pathology, researchers are starting to exploit the increased magnetic susceptibility contrast at fields above 3 T, such as 7 T, with both *in vivo* (Ge *et al*., 2008; Hammond *et al*., 2008*a*, *b*; Tallantyre *et al*., 2008, 2009, 2010, 2011; Haacke *et al*., 2009; Wattjes and Barkhof, 2009; Madelin *et al*., 2010; Metcalf *et al*., 2010) and post-mortem imaging (Pitt *et al*., 2010; Schmierer *et al*., 2010).

Magnetic susceptibility is an intrinsic property of tissue determined by molecular composition. Its effect on susceptibility-weighted gradient echo MRI techniques increases with field strength (Abduljalil *et al*., 2003; Duyn *et al*., 2007). Studies on healthy brains both *in vivo* and post-mortem suggest that magnetic susceptibility contrast has several contributors, such as myelin (Duyn *et al*., 2007; Li *et al*., 2009; Fukunaga *et al*., 2010), calcium and phospholipid (He and Yablonskiy, 2009), haem-iron (deoxyhaemoglobin) and non-haem iron (Bizzi *et al*., 1990; Schenck 1995; Gelman *et al*., 1999; St Pierre *et al*., 2005; House *et al*., 2006, 2007, 2010; Lee *et al*., 2009, 2010*a*; Shmueli *et al*., 2009; Yao *et al*., 2009; Fukunaga *et al*., 2010). Of these factors, non-haem iron and myelin are both particularly relevant with respect to multiple sclerosis pathology. Studies have indeed shown that the transverse relaxivity R_2* and frequency shifts are closely associated with iron and myelin distribution in multiple sclerosis-induced white matter lesions (Hammond *et al*., 2008*a*, *b*; Haacke *et al*., 2009; Yao *et al*., 2010).

In multiple sclerosis, iron accumulation may reflect a multiplicity of pathological and physiological processes (Craelius *et al*., 1982; Connor *et al*., 1995; Levine and Chakrabarty, 2004). Hence, iron has the unique potential to serve as an *in vivo* tracer of disease pathology. At the inflammatory site, iron may be present during both the acute and chronic phase. Free iron may be released from non-haem proteins whose degradation is induced by respiratory burst molecules produced by microglia and macrophages during acute inflammation phases. In chronic inflammation, protein–iron deposits may be contained in macrophages indicating microglia activation and chronic inflammation at the site of white matter lesions, areas adjacent to white matter lesions and the inner cortex adjacent to the white matter (Craelius *et al*., 1982). At the demyelination site, iron is released from degrading oligodendrocytes (after myelin is destroyed). Independently of its source, free iron can partake in reactions leading to toxic-free radical formation, oxidative damage and mitochondrial injury. Iron accumulation, however, may also reflect active processes of physiological myelination or reparative remyelination through its essential role as co-factor for numerous enzymes involved in lipid biosynthesis associated to myelin formation (Connor *et al*., 1996).

To investigate the feasibility of distinguishing between these various processes of iron accumulation based on MRI, the cellular localization of iron responsible for the MRI changes would need to be established. To address this issue, we combined 3 T and 7 T MRI with pathological analysis of five brain slices from three deceased donors, two of which had multiple sclerosis. The 3 T MRI was obtained only with the aim of acquiring standard clinical sequences by which regions of interest of normal white matter, normal-appearing white matter and white matter lesions were identified and compared with 7 T gradient echo R_2* and phase images. This comparison identified heterogeneous patterns of contrast on the 7 T multi-echo gradient echo R_2* and phase images. To understand the biological basis of this heterogeneity, a detailed qualitative histopathological analysis of white matter, normal-appearing white matter and white matter lesion regions of interest showing different appearances on the 7 T-gradient echo was obtained and pathological correlates of MRI findings were assessed.

Materials and methods

Study design and samples

This was a collaborative project between the National Institute of Neurological Disorders and Stroke (NINDS) at the NIH, Bethesda, MD, USA and the Centre for Brain Research of the Medical University in Vienna, Austria. A Material Transfer Agreement between the NIH and the University of Vienna was signed from both institutions.

The samples used for this study derive from two patients with multiple sclerosis, designated Patients MS-1 and MS-2 hereafter, and one non-multiple sclerosis donor. All the samples were obtained from NINDS.

Clinical histories

None of the patients were seen in the NIH-multiple sclerosis clinic. Details of their clinical history derive from the retrospective evaluation of clinical charts (F.K.C.) and from clinical history collected retrospectively from family members.

In addition, to rule out possible Alzheimer's confounder pathology, haematoxylin and eosin, Bielschowsky silver impregnation and amyloid-β and -tau AT8 stains were performed on tissues from all three cases at the Centre for Brain Research, Medical University, Vienna, Austria.

Patient MS-1, a Caucasian male, had a disease course consistent with relapsing–remitting multiple sclerosis evolving into secondary progressive multiple sclerosis. Onset of multiple sclerosis occurred at the age of 40 years with an episode of left optic neuritis. After partial recovery, the patient had 2 months of 'forgetfulness' and recovered full vision at the age of 42 years. Between the ages of 42 and 51 years, the patient had 11 clinical relapses involving the spinal cord, the brainstem and the cerebellum with varying amounts of recovery during remissions. Gradually, he developed bladder symptoms and erectile dysfunction treated with an implanted penile prosthesis. At the age of 48 years, he began using a cane and gait progressively worsened thereafter. He needed automobile hand controls at the age of 51 years, and used a scooter, wheel chair and, for a limited period of time, a walker at the age of 52 years. Subsequently, he developed progressively worse motor function, bladder control, constipation and cognitive impairment. At the age of 65 years, he was admitted to a nursing home, bedridden with a permanent Foley catheter and evidence of nutritional deterioration. By the age of 66 years, his cognitive impairment progressed to pronounced dementia. He had several episodes of sepsis due to urinary tract infections. He was described as demented with euphoria at the age of 67 years and non-verbal at the age of 70 years. He died with pneumonia at the age of 70 years in March 2005.

Spinal fluid examination at the age of 44 years was positive for oligoclonal bands. Early in his disease course, intermittent glucocorticoid treatments had been discontinued because of acute changes in mentation. He had not tolerated cyclosporine.

Apart from multiple sclerosis, this patient had labile hypertension by the age of 63 years and intermittent atrial fibrillation and non-atrial fibrillation sustained tachycardia at the age of 69 years. Chest X-ray shortly before death showed pneumonia and borderline cardiac enlargement.

At autopsy, the patient showed cardiomegaly, atherosclerosis of the aorta and coronary arteries, and prostatic adenocarcinoma *in situ*. The brain weighed 1225 g and had a smooth surface without signs of infarction. There was severe atherosclerosis of the Circle of Willis and major branches. Patient MS-1 did not fulfil Braak's histopathological for Alzheimer's diagnosis (Braak and Braak, 1997). In line with chronic multiple sclerosis pathology (Dal-Bianco *et al*., 2008), a few neurofibrillary tangles within the entorhinal cortex (basal temporal lobe) were observed. The haematoxylin and eosin staining of the hippocampus revealed profound neuronal loss in the CA1 region (sommer sector) due to hypoxic brain injury.

Case MS-2, a Caucasian female, had a disease course consistent with a relapsing–remitting multiple sclerosis rapidly progressing to secondary progressing multiple sclerosis and preponderant spinal cord involvement. She presented with right optic neuritis at the age of ~37 years. Shortly, thereafter, she had an episode of bilateral hand paraesthesias followed by an episode of gait disturbance. She developed progressively worse gait disturbance and by the age of 39 years required the use of a cane and then progressed to using a rollator. By the age of 50 years, she was restricted to a wheelchair and had poor bladder control. A baclofen pump was implanted. At the age of 59 years, her progressive disability required assistance with her activities of daily living. On physical examination, she showed spastic quadriplegia with retained ability to partially lift the arms. She had abnormal movements suggestive of dystonic posturing. In the subsequent 2 years, she required a tracheotomy and nocturnal use of a ventilator because of progressively worse dysphagia, frequent aspiration, pulmonary insufficiency and pulmonary infections. She died of pneumonia at the age of 61.5 years in February 2009. During her lifetime, she was treated with multiple courses of intravenous methylprednisolone, interferon β-1 a, interferon β-1 b, intravenous immunoglobulins, intrathecal methotrexate and autologous bone marrow stem cell transplantation. Apart from multiple sclerosis, the patient was treated for mild hypothyroidism. Autopsy showed numerous multiple sclerosis plaques in the brain and spinal cord. Microscopic examination of several plaques showed loss of myelin and oligodenrocytes, astrocytosis and a few macrophages consistent with chronic lesions. There were no signs of cerebrovascular disease. Brain weight was 1140 g with normal ventricular size.

As with Patient MS-1, Patient MS-2 did not fulfil Braak's histopathological criteria for Alzheimer's diagnosis (Braak and Braak, 1997).

The brain of the non-multiple sclerosis case was from a Caucasian male with severe combined immunodeficiency syndrome secondary to recombination activating gene 1 (RAG1) deficiency. His disease course was characterized by multiple infections and progressive granulomatous disease involving pharynx, palate, nose, skin, nasopharyngeal mucosa, lungs and colon. At 5 years of age, he was diagnosed with myasthenia gravis treated with thymectomy and had 6 years of intravenous immunoglobulin infusions. During his lifetime, he was treated with multiple courses of steroids and infliximab, cytoxan and rituximab. He had a history of drug abuse requiring three hospitalizations for overdose. Cause of death at the age of 19 years was due to overdose of phenergan and gabapentin. Autopsy of the brain showed no gross or microscopic abnormalities and brain weight was 1450 g.

Tissue collection and preparation for magnetic resonance imaging

In each case, autopsy was performed within a few hours of death and the entire brains of Patient MS-1 and the non-multiple sclerosis case were immediately fixed in 4% paraformaldehyde. Two weeks later, the brains were sectioned into 10-mm thick coronal slices. In the case of Patient MS-2, the brain was cut immediately after death and prior to fixation, due to the need for fresh tissue for unrelated studies. A few 10-mm thick coronal slices were then fixed in 4% paraformaldehyde for the imaging study.

MRIs were obtained at two (non-multiple sclerosis case), three (Patient MS-2) and 36 (Patient MS-1) months after death. For imaging, each brain slice was placed in a cylindrical, specially fabricated tissue container and imaged in 4% paraformaldehyde fluid in the container (Bagnato *et al*., 2009). A total of five 10-mm thick coronal slices were imaged: three slices from Patient MS-1 and one slice each from Patient MS-2 and the non-multiple sclerosis case.

Image acquisition and reconstruction

3 Tesla magnetic resonance imaging

Scans were acquired using a 3 T magnet (GE Medical Systems) equipped with an 8-channel receive-only head array. Dual echo T_2-weighted fast spin echo and proton density-weighted images, and 3D magnetization prepared rapid acquisition gradient echo (MP-RAGE) T_1-weighted were acquired as previously described (Bagnato *et al*., 2009). The 3 T MRI was performed to identify lesions and normal-appearing white matter areas on the basis of accepted definitions for clinical scans.

7 Tesla magnetic resonance imaging

Scans were acquired using a whole body GE Sigma 7 T MRI scanner (GE Medical Systems) using a 24-channel receive-only array designed for tissue imaging (Fukunaga *et al*., 2010). A 3D T_2*-weighted multi-echo gradient echo sequence was performed with repetition time = 200 ms, voxel resolution = 0.2 × 0.2 × 0.2 mm^3, flip angle = 20°, bandwidth = 62.5 kHz; data were acquired at multiple echo times of 8.7, 25.2, 41.7 and 58.2 ms.

Images were reconstructed using a phase-sensitive noise-weighted channel combination (Duyn *et al*., 2007). Quantitative R_2* maps were obtained using an exponential fitting to the images with different echo times. To remove phase wraps, the complex data were first smoothed by a Gaussian filter (full width at half maximum = 30 voxels) to determine the macroscopic background phase. Continuous phase maps were then generated after subtraction of the phase background from the original data. Negative phase shifts (darkening in the maps) corresponded to increased MRI resonance frequency, generally indicating the presence of paramagnetic compounds. Data processing, including image reconstruction, calculation of R_2* and phase maps, was performed with IDL 7.0 software.

Image analysis and region of interest selection

Regions of interest of normal white matter, normal-appearing white matter and white matter lesions were identified and traced in each 3 T and 7 T sequence and their conspicuity compared. For scans obtained at 3 T, white matter lesions were identified on T_2-weighted fast spin echo and proton density-weighted images as well as in the T_1-based magnetization prepared rapid acquisition gradient echo.

On the phase and R_2* images, the abnormal areas within white matter lesions and normal-appearing white matter were defined from areas with dark (hypointense) or bright (hyperintense) signal comparing to the surrounding normal-appearing white matter (Yao *et al*., 2010). The 7 T lesion identification was done by two researchers, F.B. and B.Y. In case of disagreement, the opinion of an expert senior investigator (J.D.) was requested.

Matching between magnetic resonance imaging and histology

Images of sections stained for proteolipid protein were acquired and stored as jpeg files. On a separate workstation, these images were then displayed alongside each corresponding 3 T and 7 T image for visual comparison. Hard copies of the 3 T scans were also printed out and used as a reference during each evaluation.

Histology

Histochemistry

For basic classification of demyelination in regions of interest, sections were stained with Luxol fast blue myelin staining (Division Chroma). Iron was detected with Perl's staining and 3,3′-diaminobenzidine-tetrahydrochloride (DAB) enhanced Turnbull blue staining (Meguro *et al*., 2007). Both methods were performed with deparaffinated, rehydrated formalin-fixed sections (control coronal sections: 7-μm thick, all others: 3–5-μm thick).

For Perl's staining, sections were incubated in distilled water with 1% potassium ferrocyanide and 1% hydrochloric acid (HCl) for 15 min. After rinsing with distilled water, sections were counterstained with nuclear fast red (Merck), dehydrated and coverslipped with Eukitt (Kindler). In case of DAB-enhanced Turnbull blue staining, sections were immersed in an aqueous ammonium sulphide solution (10% in distilled water) for 90 min and washed with distilled water. This process was followed by 15-min incubation with aqueous solution containing 10% potassium ferricyanide and 0.5% HCl. After five washings with distilled water, sections were incubated in methanol containing 0.01 M sodium azide and 0.3% hydrogen peroxide for 60 min. Next, sections were washed five times with 0.1 M phosphate buffer. Iron was visualized using a solution containing 0.025% DAB (Sigma Aldrich) and 0.005% hydrogen peroxide in a 0.1 M phosphate buffer for 20 min. The reaction was stopped by rinsing with tap water. Sections were dehydrated and coverslipped with Eukitt.

Immunohistochemistry

Immunohistochemical staining for myelin and oligodendrocytes [proteolipid protein and tubulin polymerization promoting protein (TPPP/p25)], astrocytes (glial fibrillary acidic protein), axons (phosphorylated neurofilament, SMI 31), microglia and macrophages (CD68), ferritin, ferritin light polypeptide (ferritin-L), amyloid-β and paired helical filament-tau (PHF-tau, clone AT8), was performed on 3- to 5-μm thick paraffin sections using the primary antibodies listed in Table 1. Before staining, endogenous peroxidase was blocked by 30-min incubation in methanol with 0.02% hydrogen peroxide. The process was followed by antigen retrieval (Table 1). Sections were then incubated with 10% foetal calf serum in DAKO rinsing buffer (Dako Cytomation). Next, primary antibodies were applied in 10% foetal calf serum/DAKO at 4°C overnight. After washing with Tris-buffered saline, secondary antibodies in foetal calf serum/DAKO were applied for 1 h at room temperature. Secondary antibodies are listed in Table 1. As a third step, sections were incubated in foetal calf serum/DAKO with avidin peroxidase (1:100; Sigma Aldrich) for 1 h. Labelling was visualized with DAB. Sections were briefly counterstained with haematoxylin, dehydrated and coverslipped with Eukitt.

Light microscopy double staining for colocalization of iron with CD68 and tubulin polymerization promoting protein

First, sections were treated using the above-mentioned DAB-enhanced Turnbull staining protocol. After developing the sections with DAB, the sections were rinsed with distilled water. Consecutive pre-treatment and primary antibody incubation was carried out after the immunohistochemistry protocol mentioned above. The antibody against TPPP/p25, a specific marker for oligodendrocytic cell bodies (Höftberger *et al*., 2010), was diluted 1:3000 in foetal calf serum/DAKO and, after overnight incubation at 4°C, applied a second time for 60 min at room temperature. For recognition of both CD68 and TPPP/p25, we applied alkaline–phosphatase conjugated donkey anti-mouse secondary antibodies (Jackson Immuno Research) for 60 min at room temperature, diluted 1:200 in foetal calf serum/DAKO. Sections were developed with fast blue (fast blue BB salt, Sigma Aldrich) and coverslipped out of water with geltol.

Confocal microscopy and double staining

Formalin-fixed, paraffin-embedded sections for immunofluorescence were treated after the immunohistochemistry protocol described above. For pre-treatment, all sections were steamed with EDTA (1 mM) in Tris-buffered saline for 60 min. Antibody diluent (DakoCytomation) was used for the background-blocking step and dilution of the primary antibodies. Since we used primary antibodies from different species

Table 1 Primary and secondary antibodies

Primary antibody (source)	Dilution of primary antibody	Secondary antibody (source)	Dilution of secondary antibody	Pre-treatment for antigen retrieval
Anti-human CD68 monoclonal mouse (Dako cytomation)	1:100	Biotinylated anti-mouse (Jackson)	1:500	60-min steam with EDTA pH 9.0
Anti-human proteolipid protein monoclonal mouse (Serotec)	1:1000	Biotinylated anti-mouse (Jackson)	1:500	60-min steam with EDTA pH 9.0
Anti-human ferritin polyclonal rabbit (Sigma)	1:1000	Biotinylated anti-rabbit (Jackson)	1:2000	60-min steam with EDTA pH 8.5
Anti-human ferritin light chain polyclonal rabbit (Proteintech)	1:100	Biotinylated anti-rabbit (Jackson)	1:2000	No pre-treatment
Anti-cow glial fibrillary acid protein polyclonal rabbit (Dako cytomation)	1:3000	Biotinylated anti-rabbit (Jackson)	1:2000	60-min steam with EDTA pH 9
Anti-phosphorylated neurofilament monoclonal mouse (SMI 31) (Sternberger Monoclonals)	1:20 000	Biotinylated anti-mouse (Jackson)	1:500	60-min steam with EDTA pH 9
Anti-TPPP/p25 monoclonal mouse (produced by Gergö Botond)	1:3000	See description of double staining and Table 2	See description of double staining and Table 2	60-min steam with EDTA in Tris buffer, pH 8.5
Anti-PHF-tau monoclonal mouse antibody, clone AT8 (Innogenetics)	1:2000	Biotinylated anti-mouse antibody (Jackson)	1:500	60-minute steam in citrate buffer, pH 6

(e.g. mouse anti-CD68 and rabbit anti-ferritin), they were applied simultaneously at 4°C overnight. After five washings with Tris-buffered saline, secondary antibodies diluted in 10% foetal calf serum/DAKO were applied simultaneously for 60 min at room temperature. Table 2 lists the secondary antibodies and dilutions used for fluorescence double labelling. The staining was completed by applying secondary antibodies or streptavidin conjugated either with Cy2 or Cy3 in 10% foetal calf serum/DAKO for 1 h. Sections were coverslipped with gallate/geltol. Fluorescent preparations were inspected and photographed using a Leica TCS SP5 confocal microscope (Leica Microsystems). Images were obtained using LAS AF software version 2.2.1 (Leica Microsystems).

Table 2 Secondary antibodies used for fluorescence stainings

Targets of primary antibodies*	Dilution	Secondary antibodies (source)	Dilution
TPPP/p25	1:1500	Biotinylated anti-mouse	1:500
+	+	+ StreptavidinCy3 (Jackson)	1:75
ferritin	1:500	donkey anti-rabbitCy2 (Jackson)	1:200
CD68	1:50	Biotinylated anti-mouse	1:500
+	+	+ StreptavidinCy3 (Jackson)	1:75
ferritin	1:500	donkey anti-rabbitCy2 (Jackson)	1:200
Ferritin light polypeptide	1:50	Biotinylated anti-rabbit	1:2000
+	+	+ StreptavidinCy2 (Jackson)	1:75
CD68	1:50	donkey anti-mouseCy3	1:200

*Same antibodies as described in Table 1.

Results

In the non-multiple sclerosis case, areas of normal white matter approved from MRI were analysed histochemically. In the cases with multiple sclerosis, four regions were selected in disease-affected areas. Conventional MRI sequences (3 T) classified three of these four regions as white matter lesions, designated WML-1, WML-2 and WML-3, and one region as normal-appearing white matter. Several important observations emerged and we present findings related to the non-multiple sclerosis donor and the cases with multiple sclerosis separately as below.

Non-multiple sclerosis donor: normal white matter

Figure 1 shows side-by-side 7 T R_2* and phase-MRI as well as the Klüver-PAS staining for myelin and total non-haem iron of the non-multiple sclerosis donor brain. The myelin pallor visible in the deep white matter and indicated by the green arrows in the Klüver-PAS staining is likely due to brain oedema possibly related to the cause of death. Across the white matter, several sources of iron were identified, all captured by striking signal changes in MRI.

First, only small amounts of iron were detected in the deep white matter structures of this brain slice. This iron, located primarily in oligodendrocytes and myelin sheaths (data not shown) generally coincided with subtle signal increase in R_2* and signal decrease in phase (Fig. 1, orange arrows).

Higher amounts of iron were found at the white matter–cortical grey matter junction in the iron staining (Fig. 1, blue arrows). Here, the iron was also located primarily within oligodendrocytes and myelin sheaths. This finding was reflected by increased R_2* and a generally decreased phase in the MRI consistent with previous work from our group (Fukunaga *et al.*, 2010).

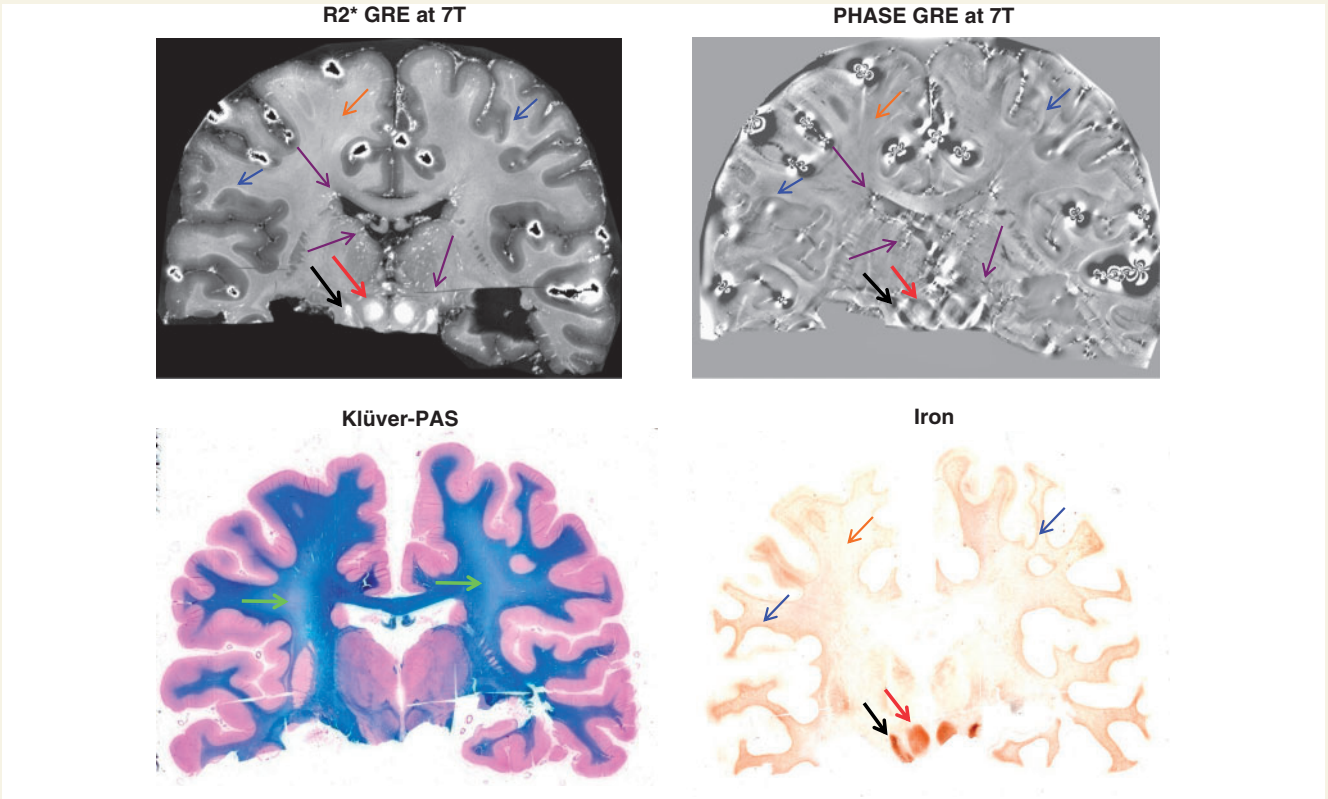

Figure 1 Non-multiple sclerosis donor brain. Coronal sections of the 19-year-old male non-multiple sclerosis Case 1. Green arrows in the Klüver-PAS staining (*bottom left*) point to areas of myelin pallor in the centrum semiovale. This pallor is likely due to brain oedema possibly related to the cause of death. In the MRI map and iron staining (*top* and *bottom right*): black arrows indicate the substantia nigra and red arrows indicate the red nucleus, both rich in iron. In the same maps, blue arrows highlight the white matter–cortical grey matter junction, which is accentuated by relatively elevated iron; brown arrows indicate deep white matter with its low–moderate iron content. In the MRI maps only (*top*), purple arrows indicate vessel-like structures, particularly seen in the regions of the deep draining veins of the brain. GRE = gradient echo.

Of note, but outside the focus of the present paper, the substantia nigra (black arrows) and the red nucleus (red arrows) in the MRI and iron maps contained the highest amounts of iron at this section level, as these nuclei were intensely stained by iron histochemistry. They are reflected by a hyperintense R_2* and varying (high/low) phase signal, consistent with earlier findings (Yao *et al*., 2009).

Streaks and spots of high R_2* and low phase signal are indicated with purple arrows in the R_2* (bright signal) and phase MRI (dark signal) (Fig. 1). These features occur particularly in large veins (thalamostriatal vein, internal cerebral vein, basal vein). However, iron histochemistry did not reveal intense perivascular iron accumulation in these regions.

Patient MS-2: normal-appearing white matter

Figure 2 shows a portion of normal-appearing white matter from Case MS-2. In general, similar to the non-multiple sclerosis donor brain, high amounts of iron were found at the white matter–cortical grey matter junction (red arrows in the iron staining). Although not as pronounced as in the normal white matter of the non-multiple sclerosis brain, this pattern was also seen in the MRI R_2* and phase data (red arrows in the R_2* and phase images).

Patchy hyperintense signal in the R_2* image matching with hypointense signal in phase-MRI was also seen in the deep normal-appearing white matter. An example of such an area is indicated by the light-blue box in the MRI maps. Iron and ferritin stainings appear to mimic the MRI data, and suggest a focal iron deposit that may have resulted from a microhaemorrhage. The latter is confirmed by a blue precipitation in the Perl's staining (Fig. 2A).

Patchy low iron content in the presence of well-preserved myelin (proteolipid protein immunohistochemistry), moderate activation of microglia (CD68 IHC) and MRI R_2* and phase changes were also seen. In some regions, noise amplification was seen in the phase image, and attributed to insufficient local sensitivity of the receive array; hence, caution needs to be taken of the interpretation of the signal in these regions. To demonstrate the cellular localization of the observed iron (high magnification), iron and TPPP/p25 as well as ferritin and TPPP/p25 stainings, obtained from the area indicated with the red box, are shown in Fig. 2B and C. In this area, iron and

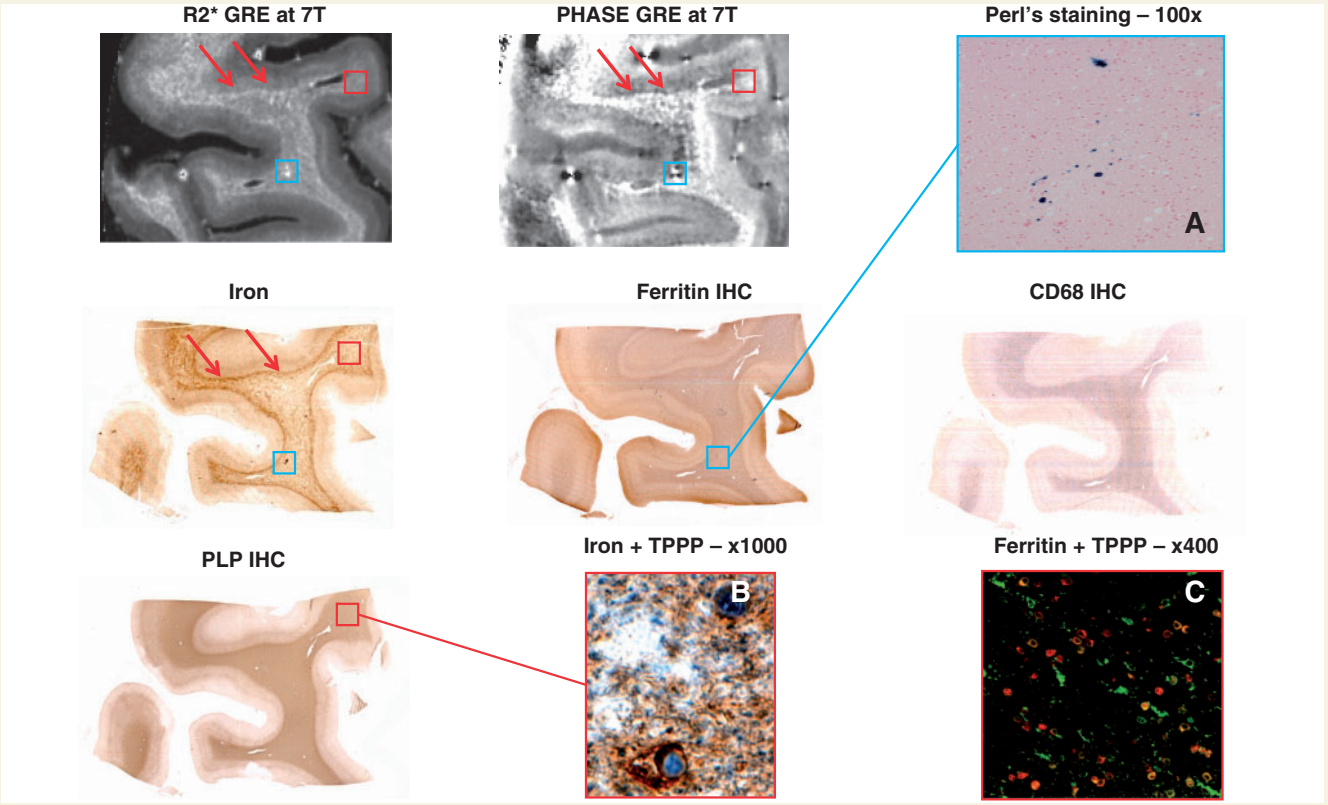

Figure 2 Normal-appearing white matter of Patient MS-2 with secondary progressing multiple sclerosis. Sections through a sample of temporal lobe of Patient MS-2 devoid of white matter lesions. In the MRI maps and iron staining (*top left*, *top centre* and *middle left*), red arrows indicate the white matter–cortical grey matter junction, whose signal is accentuated by relatively high iron content. In the same maps and in the ferritin immunohistochemistry staining (*centre*), blue boxes highlight a focus of iron accumulation. The respective area is shown at higher magnification of a slide stained with the Perl's method (**A**), which reveals haemosiderin deposition strongly suggestive of microhaemorrhage in this area. Red boxes in the MRI maps, proteolipid protein (PLP, *bottom left*) and iron stainings define the location where the double stainings (**B** and **C**) were photographed. (**B**) Double staining of iron (brown) and TPPP/p25 (blue). (**C**) Confocal microscopy double-staining of ferritin (green) and TPPP/p25 (red). Co-localization is rendered in yellow. GRE = gradient echo; IHC = immunohistochemistry.

ferritin were found within oligodendrocytes and myelin sheaths. As a demonstration of the former, the double staining of iron (brown) and the oligodendrocyte marker TPPP/p25 (blue) show how oligodendrocytes store iron within their cytoplasm. The double staining confocal microscopy of ferritin (green) and TPPP/p25 (red) indicates that many, although not all, of the ferritin-containing cells are oligodendrocytes. However, there are also cells with microglial morphology expressing ferritin in this region (green branched cells), and also virtually ferritin-free oligodendrocytes.

Patient MS-1: white matter lesions

White matter lesion classification by magnetic resonance imaging and histopathology

Figures 3–5 show side by side, the appearance of the three selected white matter lesions, namely WML-1, WML-2 and WML-3, in 7 T R_2* and phase-MRI as well as the corresponding stains for non-haem iron, ferritin, ferritin-L, activated microglia and macrophages (CD68), and myelin (proteolipid protein).

Conventional MRI sequences at 3 T classified all three lesions as chronic lesions due to their hyperintense signal in T_2-weighted images and their hypointense signal in the T_1-based magnetization prepared rapid acquisition gradient echo (images not shown).

By histopathology, all three white matter lesions were classified as slowly expanding lesions (Lassmann, 2008). The core of all three white matter lesions showed complete demyelination detected by proteolipid protein staining, moderate axonal rarefication (phosphorylated neurofilament staining, data not shown), astroglial scar tissue (glial fibrillary acid protein staining, not shown) and sparse inflammatory infiltrates (CD68 staining). The white matter lesion rim showed microglia and macrophage activation as seen from CD68 upregulation, and low to moderate demyelinating activity, assessed by myelin degradation products within the lysosomes of macrophages visualized by Klüver-PAS staining (data not shown). WML-2 was a coalescing lesion with sparse demyelinating activity at the site of coalescence, which is marked by the blue arrows in Fig. 4. The outer edges of the lesion (red arrows) were inactive.

Qualitative comparisons between magnetic resonance imaging and histopathology

The three white matter lesions analysed generally showed low MRI R_2* and variable phase, while histopathology indicated absent myelin and low or absent iron. More detailed inspection revealed the following three patterns.

In the core of each white matter lesion, at least one large vessel with thickened media and perivascular iron accumulation was seen. The presence of such a vessel was indicated on MRI by high R_2* and low phase as noted with the blue arrows in the magnetic resonance, iron, ferritin and ferritin-L images of Figs 3–5 and blue squares in the iron and ferritin images of Fig. 3 or in the proteolipid protein image of Fig. 4. WML-1 in Fig. 3 shows a large vessel with particularly intense perivascular iron accumulation being detected by a blue precipitation in the Perl's reaction, which is highly suggestive of haemorrhage. This site of iron deposition is detected by high R_2* and low phase as indicated by the blue arrows. Similarly, in WML-2, these vessels showing perivascular iron accumulation are displayed in the higher magnification of the iron staining (Fig. 4A and B). The iron around the vessels seems to be deposited within microglia and macrophages but also diffusely dispersed within the extracellular space.

The second observation in the three white matter lesions were streaks and small rings of high R_2* and variable phase changes, as indicated by the green arrows in the R_2* and phase images of Figs 3 and 4. These streaks resemble the structures found in the non-multiple sclerosis donor brain (Fig. 1, purple arrows). These streaks coincide with large vessels identified on the histological stainings and appear not accompanied by histochemically detectable iron accumulation, as it is the case with the non-multiple sclerosis donor brain.

The third observation is within the lesional rims. In all the white matter lesions, the rims were partly accentuated by high R_2* and low phase. This is most prominent in WML-1 and WML-3, as indicated by red arrows in Figs 3 and 5. This MRI signal almost invariably matched with iron and ferritin accumulation together with high CD68 immunoreactivity. The bottom of WML-3 comprises a rim, which showed upregulated CD68, but neither sparse ferritin or iron accumulation, nor prominent MRI signal changes. Figure 3B–D illustrates a strongly CD68-positive typical active rim

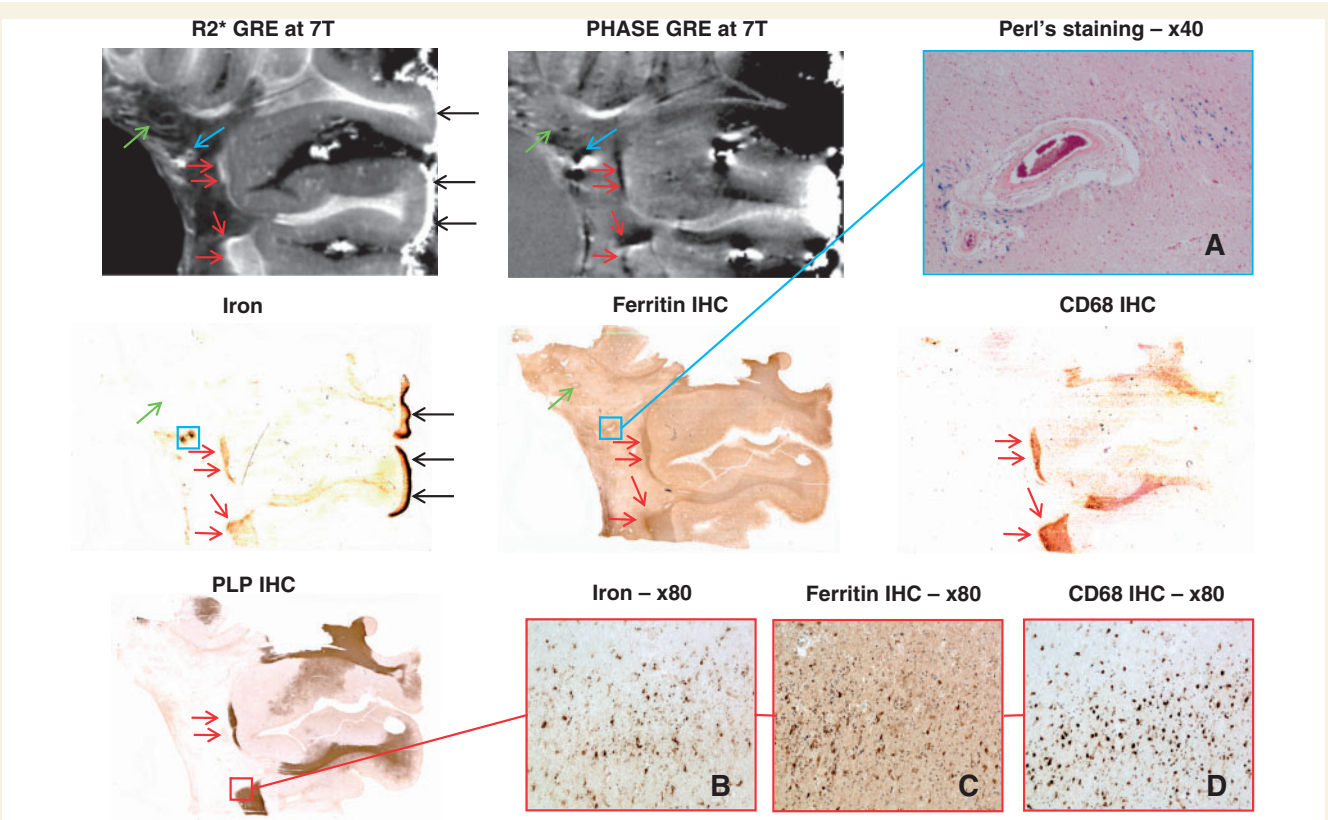

Figure 3 Slowly expanding WML-1 and normal-appearing white matter of Patient MS-1 with secondary progressing multiple sclerosis. Sections through a sample from Patient MS-1 with a periventricular white matter lesion. Red arrows in the MRI maps (*top centre* and *left*), iron, ferritin, CD68 and proteolipid protein (PLP) stainings (*middle left*, *centre*, *middle right* and *bottom left*, respectively) indicate the lesional edges showing low–moderate demyelinating activity. Red box in the proteolipid protein staining defines the area where images **B–D** depict such an edge at higher magnification. Blue arrows in the MRI maps and blue boxes in the iron and ferritin stainings indicate a large vessel with thickened media and perivascular iron accumulation. (**A**) Perl's staining of this vessel reveals haemosiderin deposition. Green arrows in the MRI maps and in the iron and ferritin stainings point towards streaks and small rings of high R_2* and variable phase, which matched with vessels found by histology. Black arrows indicate high amounts of iron located subpially, which are very likely an artefact due to long formalin fixation. GRE = gradient echo; IHC = immunohistochemistry.

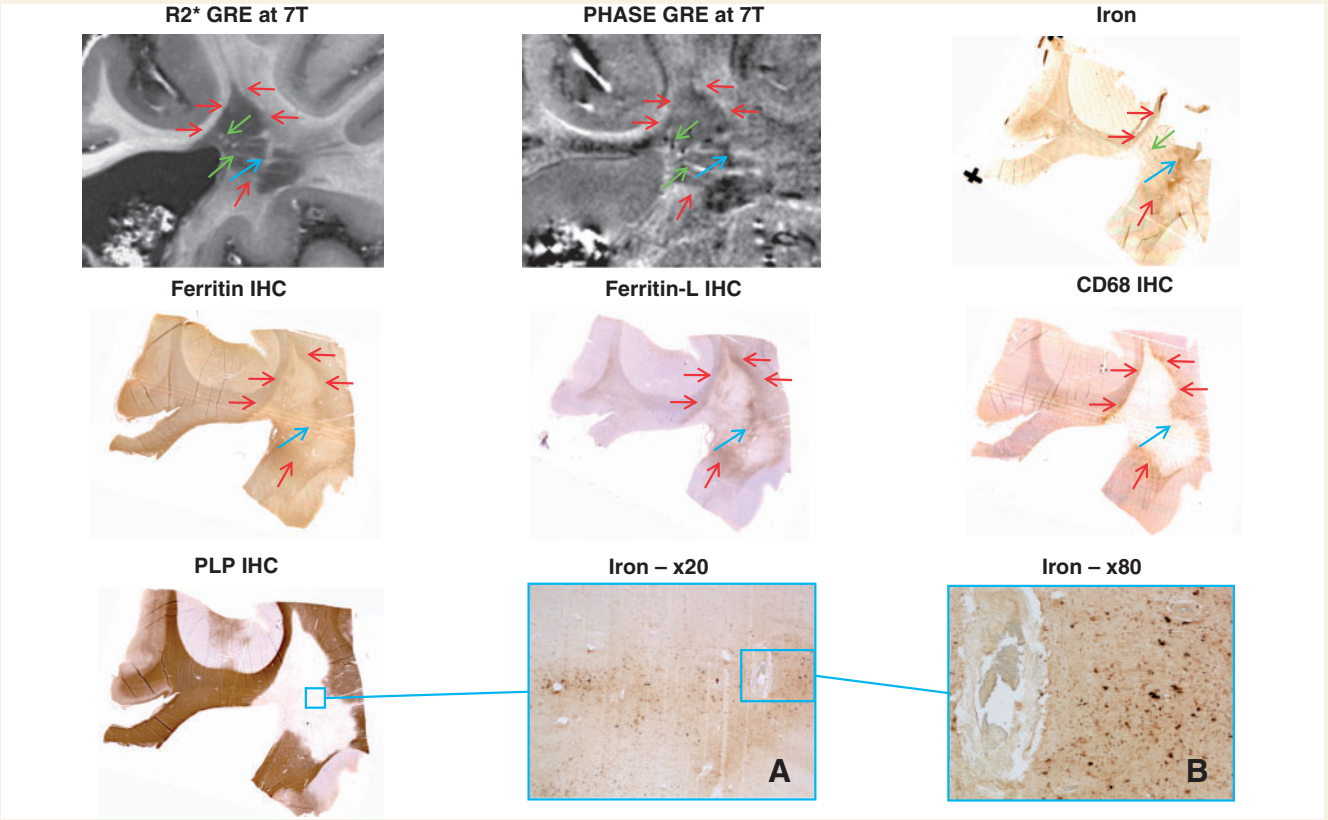

Figure 4 Slowly expanding WML-2 and normal-appearing white matter of Patient MS-1 with secondary progressing multiple sclerosis. Sections through a sample from Patient MS-1 adjacent to the lateral ventricle showing a periventricular white matter lesion. This confluent lesion presented with virtually absent demyelinating activity at the edge, indicated by the red arrows in MRI maps (*top centre* and *left*) and all stainings [but proteolipid protein (PLP)]. Blue arrows and boxes highlight area of low demyelinating activity and perivascular iron accumulation around a vessel with thickened media, which is depicted at higher magnification by **A** and **B**. Green arrows in MRI maps and iron staining point towards streaks and small rings of high R_2* and variable phase which matched with vessels found by histology. GRE = gradient echo; IHC = immunohistochemistry.

with high iron and ferritin contents at higher magnification. WML-2 showed iron and ferritin-L accumulation together with MRI signal changes at the site of coalescence and low activity (blue arrows in Fig. 4).

The black arrows in Figs 3 and 5 point to particularly intense iron reactivity, which was located subpially within gyri but not sulci. Microscopically, the iron was mainly present within the nuclei of virtually all cells, including neurons (data not shown). The double staining in Fig. 5A showing iron (brown) and CD68 (blue) indicates that cells enriched in iron are microglia and macrophages, although not all the microglia and macrophages seem to be iron enriched cells. The confocal microscopy double staining (Fig. 5B) reveals co-localization of ferritin (green) and CD68 (red), indicating that many microglia and macrophages upregulate ferritin within the rim of this lesion.

Discussion

Two main observations arise from the present study. The first one is that in multiple sclerosis tissue, iron invariably resulted in R_2* increase. However, increased R_2* was not always associated with the presence of iron on histochemical staining. The second observation is that iron was present in a variety of cell types. In this section, we will elaborate on these findings. We will then conclude by addressing the study limitations and highlighting the potential impact of our findings in the clinic.

Oligodendrocytes as source of iron producing signal change by R_2*/phase multi-gradient echo maps

The qualitative analysis of the normal white matter of the non-multiple sclerosis case and the normal-appearing white matter of Patient MS-2 suggests that iron is primarily stored in ferritin residing in oligodendrocytes and microglia. In our samples, iron was present within oligodendrocytes and myelin sheaths at the cortical/subcortical junction as well as in deeper white matter. From a histopathological standpoint, this is not a novel observation in normal white matter. Oligodendrocytes, highly dependent on iron availability for their normal functionality (Gerber *et al.*, 1989; Connor and Menzies, 1996), are known to be the major iron-containing cells in the adult CNS (Connor and Menzies,

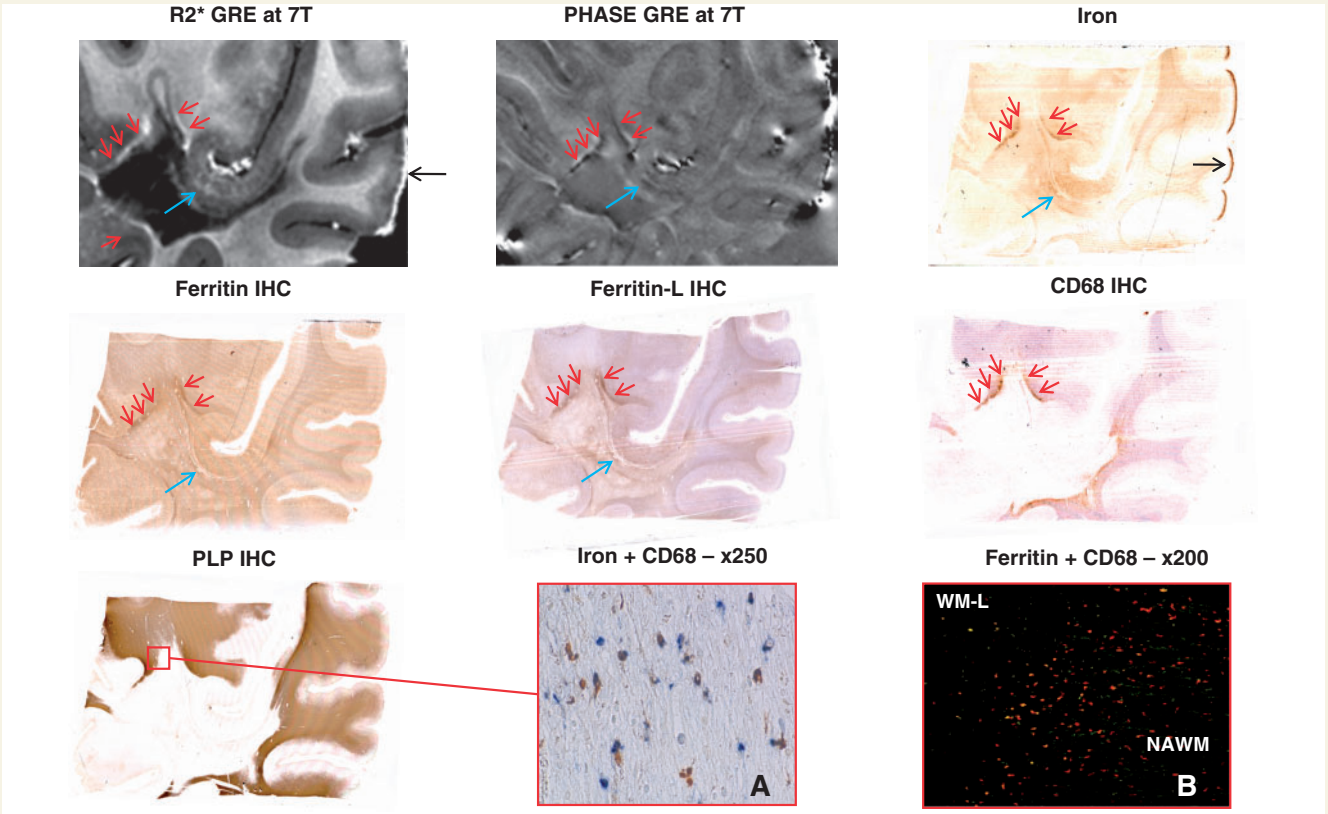

Figure 5 Slowly expanding WML-3 and normal appearing matter of Patient MS-1 with secondary progressing multiple sclerosis. Sections through a piece of temporal lobe from Patient MS-1 showing a white matter lesion. Red arrows in MRI maps (*top centre* and *left*) and all stainings [but proteolipid protein (PLP)] indicate lesion edges showing low–moderate demyelinating activity. Black arrows in the R_2* image and iron staining point towards subpial iron accumulation, which is likely due to long formalin fixation. Red box in proteolipid protein staining defines the region where images **A** and **B** were taken. (**A**) Double staining of iron (brown) and CD68 (blue). (**B**) Confocal microscopy double staining of ferritin (green) and CD68 (red). Co-localization is rendered in yellow. Blue arrows point towards vessels with thickened media showing some iron accumulation located perivascularily. GRE = gradient echo; IHC = immunohistochemistry.

1996). In the normal-appearing white matter of our rapidly progressive multiple sclerosis case (Patient MS-2), the co-localization of iron and ferritin within the oligodendrocytes, therefore, suggests a continued presence of functioning oligodendrocytes despite the pathology. The presence of iron in the cortical–subcortical junction was shown with MRI by focal R_2* and phase changes in both normal white matter and normal-appearing white matter. In contrast, a more diffuse and faint MRI contrast pattern appears to reflect the presence of iron in the oligodendrocytes of the deep white matter. Two main factors may explain this phenomenon. First, the different level of complexity of white matter fibre organization between the cortical–subcortical junction and the deep white matter, with the former less organized and compact than the latter. Secondly, the amount of iron at the junction between the cortex and the white matter, known to be greater than in the deep white matter. This elevated subcortical iron has been reported in several earlier studies (Spatz, 1922; Drayer *et al*., 1986; Curnes *et al*., 1988). The reason for this finding is currently unknown. Epigenetic differences of subcortical oligodendrocytes may play a role, since in our tissues oligodendrocytes frequently showed stronger cytoplasmic iron reactivity within the cortex than in white matter (data not shown).

A patchy appearance of iron on MRI in the normal-appearing white matter tissue of our patient with secondary progressing multiple sclerosis (Patient MS-2) was confirmed by the histochemical demonstration of the presence of iron-free oligodendrocytes mixed with iron-enriched ones. Such an observation has been reported previously in white matter of normal brains (Connor and Menzies, 1996; Todorich *et al*., 2009) and therefore is not specifically indicative of multiple sclerosis. Although the functional significance of the patchy iron distribution is not known, it is likely that again epigenetic factors play a role so to that iron is primarily located in myelinating foci, which in turn, are patchily distributed around vessels (Burdo *et al*., 1999).

Microglia iron-enriched cells as source signal change by R_2*/phase multi-gradient echo maps within non-lesional tissue

The second observation we made from the normal-appearing white matter tissue of our patient with rapidly progressive multiple

sclerosis (MS-2) was that activated microglial cells also appeared to be enriched with ferritin and iron. Since ferritin and iron signals co-localized, it is likely that those cells were filled with iron as well. Hence, it is plausible that the increased MRI R_2* and the decreased phase seen in the deep white matter of Patient MS-2 tissue co-localized with iron in microglia. Nonetheless, the MRI signal was by no means specific enough to capture the differences between iron-enriched microglia and oligodendrocytes. The latter is an important drawback of MRI. Indeed, while iron-enriched oligodendrocytes are a sign of healthy tissue, iron-enriched microglia may indicate the presence of ongoing disease.

Microglia iron-enriched cells as source signal change by R_2*/phase multi-gradient echo maps within white matter lesion rim

Ferritin- and iron-enriched activated microglia/macrophages were also found surrounding the core of the WML-1 and -3 of the case with secondary progressing multiple sclerosis (Patient MS-1) as shown by the presence of R_2* bright and phase dark signal in multi-gradient echo images. However, in WML-3 the rim at the bottom of the images showed upregulated CD68 in the absence of prominent MRI signal changes, ferritin upregulation and iron accumulation. Two explanations may be provided to understand this finding. First, microglia mainly take up iron that has been liberated during the course of demyelination. Hence, the level of iron accumulation of a demyelinating lesion edge would be dependent upon the amount of iron in the adjacent oligodendrocytes. Secondly, different subpopulations of microglia with a different propensity to iron accumulation may be present. Whereas it has been shown that iron influences functions of activated microglia (Mairuae *et al*., 2011), control of iron homoeostasis in microglia remains poorly understood (Ward *et al*., 2011). The presence of activated microglia around the demyelinated core of white matter lesions has already been defined as the hallmark of slowly expanding lesions (Prineas *et al*., 2001; Lassmann *et al*., 2007). When iron is released from oligodendrocytes as it may happen during demyelination and cellular degeneration, in general, it may become exposed to proteases in the extracellular space. Additional acidification of the inflammatory environment within the tissue facilitates the transformation of Fe^{3+} into Fe^{2+}. The presence of Fe^{2+} is implicated in reactions involving oxygen and nitric oxide radicals, which may contribute to mitochondrial dysfunction and neurotoxicity (Bolanos *et al*., 1997; Smith *et al*., 1997). In response, macrophages take up the iron, transform it into Fe^{3+} and bind it to their ferritin, thus causing detoxification of the tissue. It is important to highlight that this process is non-specific to multiple sclerosis. Similar processes have been suggested to occur in Alzheimer's disease plaques (Lopes *et al*., 2008) and Huntington's disease (Simmons *et al*., 2007).

Patchy isolated foci of R_2* increased and phase decreased signal correspond to iron precipitation in aggregates within normal-appearing white matter and white matter lesions

Within the normal-appearing white matter of our female patient with secondary progressing multiple sclerosis, but also in the core of white matter lesions of our case with secondary progressing multiple sclerosis, MRI identified patchy isolated foci of increased R_2* and decreased phase. These changes corresponded to intense iron precipitation in aggregates typical of microbleeds as shown by Perl's staining. The relation between the topography of multiple sclerosis and vessel architecture has been demonstrated by pathological studies (Fog, 1964). The presence of haemosiderin inside and outside multiple sclerosis plaques has also been described previously (Adams, 1988). Haemosiderin deposition is considered a sign of remote haemorrhage. Capillary haemorrhages have been described as multiple sclerosis features (Craelius *et al*., 1982; Adams, 1988) although not consistently across all the examined samples (Walton and Kaufmann, 1984). Haemosiderin deposition may be occasionally seen in 'normal' brain (Adams, 1988) as well as in brains of patients with cardiovascular diseases (Adams, 1988). Under these conditions, however, haemosiderin tends to be spread within the white matter. Conversely, the patchy localization of haemosiderin in the vicinity of plaques has led researchers to attribute a pathogenic role to capillary and venous haemorrhages in multiple sclerosis (Adams, 1988). Specifically, it has been hypothesized that the damage around the veins, severe enough to cause permeability changes and haemorrhage, is an important component of multiple sclerosis (Adams, 1988).

Clearly, the small number of examined tissues does not permit us to draw conclusions about the possible pathogenic role of small haemorrhagic foci in multiple sclerosis. Care needs to be exercised in interpreting our findings also in relation to other systemic diseases. For instance, in Patient MS-1, who had cardiovascular disease, haemosiderin aggregates were found within the white matter lesions. Vascular disease, and not necessarily multiple sclerosis, may have caused these aggregates. These changes, which may be partially due to vascular disease, are not likely to be found in young patients with multiple sclerosis without cardiovascular risk factors when imaged *in vivo*. Yet the findings remain a clear demonstration that these foci can be an additional source of MRI signal changes in R_2* and phase images when one attempts to analyse the brain of patients with multiple sclerosis using multi-gradient echo.

R_2* and phase signal changes in regions of deep brain veins are not matched by iron histochemistry

In normal white matter, normal-appearing white matter and also in white matter lesions, we observed R_2* and phase changes in regions of deep brain veins identified histologically. These MRI signal changes, although suggestive of iron, were not confirmed

by the DAB-enhanced Turnbull blue staining. We postulate that the lack of cross-linking with proteins of the iron possibly present at this level might be responsible for the findings. More specifically, we hypothesize that when iron is no longer bound to protein (ferritin) and when it is transferred to Fe^{2+} due to the acidic extracellular environment, it may become washed out during paraffin embedding and staining procedures. The histological detection of iron is challenging and histology may underestimate the actual levels of iron (Erb *et al*., 1996). The latter could explain why bright signals in R_2* MRI maps, which were taken before the embedding, sectioning and staining procedure, were no longer reflected by iron presence in the sections, which were obtained after these procedures. Another possibility one could argue to explain the MRI signals unmatched by iron staining, is the presence of susceptibility artefacts from air around vessels trapped during fixation and embedding. However, it seems unlikely to the authors that air would distribute in such a homogenous and symmetrical manner.

Subpial iron accumulation was present in Case MS-1

Subpial iron, indicated by a diffused bright signal in R_2* map (of Case MS-1 as an example), was detected. Iron was found primarily within nuclei of cells including neurons, and is most likely an artefact caused by a leaking out process due to the use of formalin. It has been reported that formalin leaches out iron from the brain and other tissues in a time-dependent manner (Smith *et al*., 1997). An experimental approach using atomic absorption spectroscopy revealed that a formalin fixation lasting 4 years leads to an average brain iron reduction of 43% (Schrag *et al*., 2010), although some studies have suggested a smaller effects (Chuaanusorn *et al*., 1997; Gellein *et al*., 2008). At the time of imaging, the brain of Case MS-1 had been stored in formalin for 3 years, compared with 3 months for Case MS-2 and 2 months for the non-multiple sclerosis donor. Spatz (1922) reported that during longstanding formalin fixation, iron not only leaches out into the formalin fluid, but also diffuses towards the surface of the tissue block. Therefore, it seems likely that this iron comes from the inner parts of the block, where it was solved out.

Study limitations

Several important study limitations bearing upon our conclusions merit discussion.

First, a technical pitfall common to all combined pathological and imaging studies is that, although the image resolution achieved with our scans was very high, MRI sections were much larger than histology sections, 0.2-mm and 5-μm thick, respectively. Accordingly, in an MRI region of interest of 0.2-mm thick, one could see focal areas of iron accumulation that were not in the plane of the section analysed histologically.

Second, MRI and histology planes were not necessarily perfectly parallel. This could explain why in WML-2, MRI signal changes were not perfectly matched by iron or ferritin light chain staining.

Third, our analysis was limited to two cases with multiple sclerosis. Hence, we cannot unambiguously rule out that other sources of iron might be present in multiple sclerosis-affected brains and we were unable to capture these because of the small sample size. Questions remain on how those sources of iron would affect MRI signal. Additionally, one cannot also exclude the possibility that signal changes in R_2* and phase images might be due to other elements that we failed to identify in our samples.

Fourth, we recognized that besides disease-specific processes such as iron accumulation and myelin loss, geometry-related factors like white matter fibre orientation and tissue microstructure, may contribute to the phase image contrast (Lee *et al*., 2010, 2011*b*; Liu 2010). Not all these components could be analysed in the context on the present study.

Fifth, as previously noted by other authors (Pitt *et al*., 2010), phase contrast is reduced post-mortem in multiple sclerosis samples. The mechanisms underlying this phenomenon are not completely known, and may complicate the correlation of post-mortem MRI with histopathology.

Last, care needs to be taken while translating our post-mortem findings into *in vivo* imaging application. Indeed, an important source of iron visible in R_2* and phase images *in vivo* may result from the presence of deoxyhaemoglobin, which was virtually absent in our specimens.

Conclusions

Our combined imaging and pathological study shows that multi-gradient echo MRI is particularly sensitive in identifying iron in the brain tissue of patients with multiple sclerosis, and indicates that localization of ferritin and assessment of iron load (e.g. white matter lesion edge > normal-appearing white matter > white matter lesion core) may be possible *in vivo*. The use of high-resolution multi-gradient echo represents an important step forward in characterization of white matter pathology in multiple sclerosis by MRI with increased specificity. While presence of iron may not be a marker sensitive only to multiple sclerosis and specific of only one pathological process, its identification by multi-gradient echo in diseased tissues can shed light on the pathological processes when coupled with topographical information and patient disease history.

Acknowledgements

The Investigators are grateful to all the patients for the precious donation of their brains to NIH for research studies and to their families for providing all clinical information required for the completeness of this work. We are indebted to the nurses Mrs Joan Ohayon and Helen Griffith (NIB–NINDS–NIH) as well as Dr Martha Quezado (National Cancer Institute, NIH) for their assistance with post mortem brains, Ms Christina Chen (NIB–NINDS–NIH) for aid in preparing the tissue for staining, Dr Nancy Richert (NIB–NINDS–NIH) for her critical revisions of the manuscript, Dr Jacco de Zwart (LFMI–NINDS–NIH) for assistance with scanning and post-processing and Ms Marianne Leiszer and Ulrike Köck (Center for Brain Research, Medical University, Vienna, Austria) for expert technical assistance with histopathological analysis.

Funding

Intramural Research Program of the NINDS, NIH and by the Austrian Science Fund (FWF Project P19854-B02).

REFERENCES

Abduljalil AM, Schmalbrock P, Novak V. Chakeres distilled water. Enhanced gray and white matter contrast of phase susceptibility-weighted images in ultra-high-field magnetic resonance imaging. J Magn Reson Imaging 2003; 18: 284–90.

Adams CW. Perivascular iron deposition and other vascular damage in multiple sclerosis. JNNP 1988; 51: 260–5.

Bagnato F, Jeffries N, Richert ND, Stone RD, Ohayon JM, McFarland HF, et al. Evolution of T1 black holes in patients with multiple sclerosis imaged monthly for 4 years. Brain 2003; 126: 1782–9.

Bagnato F, Yao B, Cantor F, Merkle H, Condon E, Montequin M, et al. Multisequence-imaging protocols to detect cortical lesions of patients with multiple sclerosis: observations from a post-mortem 3 Tesla imaging study. J Neurol Sci 2009; 282: 80–5.

Bizzi A, Brooks RA, Brunetti A, Hill JM, Miletich RS, Francavilla TL, et al. Role of iron and ferritin in MR imaging of the brain: a study in primates at different field strengths. Radiology 1990; 177: 59–65.

Bolanos JP, Almeida A, Fernández E, Medina JM, Land JM, Clark JB, et al. Potential mechanisms for nitric oxide-mediated impairment of brain mitochondria energy metabolism. Biochem Soc Trans 1997; 25: 944–9.

Braak H, Braak E. Diagnostic criteria for neuropathologic assessment of Alzheimer's disease. Neurobiol Aging 1997; 18: 85–8.

Burdo JR, Martin J, Menzies SL, Dolan KG, Romano MA, Fletcher RJ, et al. Cellular distribution of iron in the brain of the Belgrade rat. Neuroscience 1999; 93: 1189–96.

Chua-anusorn W, Webb J, Macey DJ, Pootrakul P, St Pierre TG. The effect of histological processing on the form of iron in ironloaded human tissues. Biochim Biophys Acta 1997; 1360: 255–61.

Connor JR, Menzies SL. Relationship of iron to oligodendrocytes and myelination. Glia 1996; 17: 83–93.

Connor JR, Pavlick G, Karli D, Menzies SL, Palmer C. A histochemical study of iron-positive cells in the developing rat brain. J Comp Neurol 1995; 355: 111–23.

Craelius W, Migdal MW, Luessenhop CP, Sugar A, Mihalakis I. Iron deposits surrounding multiple sclerosis plaques. Arch Pathol Lab Med 1982; 106: 397–9.

Curnes JT, Burger PC, Djang WT, Boyko OB. MR imaging of compact white matter pathways. Am J Neuroradiol 1988; 9: 1061–8.

Dal Bianco A, Bradl M, Frischer J, Kutzelnigg A, Jellinger K, Lassmann H. Multiple sclerosis and Alzheimer's disease. Ann Neurol 2008; 63: 174–83.

Drayer B, Burger P, Darwin R, Riederer S, Herfkens R, Johnson GA. MRI of brain iron. AJR Am J Roentgenol 1986; 147: 103–10.

Duyn JH, van Gelderen P, Li TQ, de Zwart JA, Koretsky AP, Fukunaga M. High-field MRI of brain cortical substructure based on signal phase. Proc Natl Acad Sci USA 2007; 104: 11796–801.

Erb GL, Osterbur DL, LeVine SM. The distribution of iron in the brain: a phylogenetic analysis using iron histochemistry. Brain Res Dev Brain Res 1996; 93: 120–8.

Fog T. On the vessel-plaque relationship in the brain of multiple sclerosis. Acta Neurol Scand Suppl 1964; 40 (Suppl 10): 9–15.

Fukunaga M, Li TQ, van Gelderen P, de Zwart JA, Shmueli K, Yao B, et al. Layer-specific variation of iron content in cerebral cortex as a source of MRI contrast. Proc Natl Acad Sci USA 2010; 107: 3834–9.

Ge Y, Zohrabian VM, Grossman RI. Seven-Tesla magnetic resonance imaging: new vision of microvascular abnormalities in multiple sclerosis. Arch Neurol 2008; 65: 812–6.

Gellein K, Flaten TP, Erikson KM, Aschner M, Syversen T. Leaching of trace elements from biological tissue by formalin fixation. Biol Trace Elem Res 2008; 121: 221–5.

Gelman N, Gorell JM, Barker PB, Savage RM, Spickler EM, Windham JP, et al. MR imaging of human brain at 3.0 T: preliminary report on transverse relaxation rates and relation to estimated iron content. Radiology 1999; 210: 759–67.

Gerber MR, Connor JR. Do oligodendrocytes mediate iron regulation in the human brain? Ann Neurol 1989; 26: 95–8.

Haacke EM, Makki M, Ge Y, Maheshwari M, Sehgal V, Hu J, et al. Characterizing iron deposition in multiple sclerosis lesions using susceptibility weighted imaging. J Magn Reson Imaging 2009; 29: 537–44.

Hammond KE, Lupo JM, Xu D, Metcalf M, Kelley DA, Pelletier D, et al. Development of a robust method for generating 70 T multichannel phase images of the brain with application to normal volunteers and patients with neurological diseases. Neuroimage 2008a; 39: 1682–92.

Hammond KE, Metcalf M, Carvajal L, Okuda DT, Srinivasan R, Vigneron D, et al. Quantitative in vivo magnetic resonance imaging of multiple sclerosis at 7 Tesla with sensitivity to iron. Ann Neurol 2008b; 64: 707–13.

He X, Yablonskiy DA. Biophysical mechanisms of phase contrast in gradient echo MRI. Proc Natl Acad Sci USA 2009; 106: 13558–63.

Höftberger R, Fink S, Aboul-Enein F, Botond G, Olah J, Berki T, et al. Tubulin polymerization promoting protein (TPPP/p25) as a marker for oligodendroglial changes in multiple sclerosis. Glia 2010; 58: 1847–57.

House MJ, St Pierre TG, Foster JK, Martins RN, Clarnette R. Quantitative MR Imaging R2 relaxometry in elderly participants reporting memory loss. AJNR Am J Neuroradiol 2006; 27: 430–9.

House MJ, St Pierre TG, Kowdley KV, Montine T, Connor J, Beard J, et al. Correlations of proton transverse relaxation rates (R2) with iron concentrations in post mortem brain tissue from Alzheimer disease patients. Magn Reson Med 2007; 57: 172–8.

House MJ, St Pierre TG, Milward EA, Bruce DG, Olynyk JK. Relationship between brain R(2) and liver and serum iron concentrations in elderly men. Magn Reson Med 2010; 63: 275–81.

Lassmann H. The pathologic substrate of magnetic resonance alterations in multiple sclerosis. Neuroimaging Clin N Am 2008; 18: 563–76.

Lassmann H, Bruck W, Lucchinetti C. The immunopathology of multiple sclerosis: an overview. Brain Pathol 2007; 17: 210–8.

Lee J, Hirano Y, Fukunaga M, Silva AC, Duyn JH. On the contribution of deoxy-hemoglobin to MRI gray-white matter phase contrast at high field. Neuroimage 2010a; 49: 193–8.

Lee J, Shmueli K, Fukunaga M, van Gelderen P, Merkle H, Silva AC, et al. Sensitivity of MRI resonance frequency to the orientation of brain to tissue microstructure. Proc Natl Acad Sci USA 2010b; 107: 5130–5.

Lee J, vanGelderen P, Kuo LW, Merkle H, Silva AC, Duyn JH. T(2)*-based fiber orientation mapping. Neuroimage 2011; 57: 225–34.

Levine SM, Chakrabarty A. The role of iron in the pathogenesis of experimental allergic encephalomyelitis and multiple sclerosis. Ann N Y Acad Sci 2004; 1012: 252–66.

Liu C. Susceptibility tensor imaging. Magn Reson Med 2010; 63: 1471–7.

Li TQ, Yao B, van Gelderen P, Merkle H, Dodd S, Talagala L, et al. Characterization of T(2)* heterogeneity in human brain white matter. Magn Reson Med 2009; 62: 1652–7.

Lopes KO, Sparks DL, Streit WJ. Microglial dystrophy in the aged and Alzheimer's disease brain is associated with ferritin immunoreactivity. Glia 2008; 56: 1048–60.

Madelin G, Oesingmann N, Inglese M. Double Inversion Recovery MRI with fat suppression at 7 tesla: initial experience. J Neuroimaging 2010; 20: 87–92.

Mairuae N, Connor JR, Cheepsunthorn P. Increased cellular iron levels affect matrix metalloproteinase expression and phagocytosis in activated microglia. Neurosci Lett 2011; 400: 36–40.

Meguro R, Asano Y, Odagiri S, Li C, Iwatsuki H, Shoumura K. Non-heme-iron histochemistry for light and electron microscopy: a historical, theoretical and technical review. Arch Histol Cytol 2007; 70: 1–19.

Metcalf M, Xu D, Okuda DT, Carvajal L, Srinivasan R, Kelley DA, et al. High-resolution phased-array MRI of the human brain at 7 Tesla: initial experience in multiple sclerosis patients. J Neuroimaging 2010; 20: 141–7.

Pitt D, Boster A, Pei W, Wohleb E, Jasne A, Zachariach CR, et al. Imaging cortical lesions in multiple sclerosis with ultra-high field magnetic resonance imaging. Arch Neurol 2010; 67: 812–8.

Prineas JW, Kwon EE, Cho ES, Sharer LR, Barnett MH, Oleszak EL, et al. Immunopathology of secondary-progressive multiple sclerosis. Ann Neurol 2001; 50: 646–57.

Schenck JF. Imaging of brain iron by magnetic resonance: T2 relaxation at different field strengths. J Neurol Sci 1995; 134 (Suppl): 10–8.

Schmierer K, Parkes HG, So PW, An SF, Brandner S, Ordidge RJ, et al. High field (9.4 Tesla) magnetic resonance imaging of cortical grey matter lesions in multiple sclerosis. Brain 2010; 133: 858–67.

Schrag M, Dickson A, Jiffry A, Kirsch D, Vinters HV, Kirsch W. The effect of formalin fixation on the levels of brain transition metals in archived samples. Biometals 2010; 23: 1123–27.

Shmueli K, de Zwart JA, van Gelderen P, Li TQ, Dodd SJ, Duyn JH. Magnetic susceptibility mapping of brain tissue in vivo using MRI phase data. Magn Reson Med 2009; 62: 1510–22.

Simmons DA, Casale M, Alcon B, Pham N, Narayan N, Lynch G. Ferritin accumulation in dystrophic microglia is an early event in the development of Huntington's disease. Glia 2007; 55: 1074–84.

Smith MA, Harris PL, Sayre LM, Perry G. Iron accumulation in Alzheimer disease is a source of redox-generated free radicals. Proc Natl Acad Sci USA 1997; 94: 9866–8.

Spatz H. Über den Eisennachweis im Gehirn, besonders in Zentren des extrapyramidal-motorischen Systems. Z Ges Neurol Psychiat 1922; 77: 261–390.

St Pierre TG, Clark PR, Chua-Anusorn W. Measurements and mapping of liver iron concentrations using magnetic resonance imaging. Cooley's Anemia Eight Symp 2005; 1054: 379–85.

Tallantyre EC, Brookes MJ, Dixon JE, Morgan PS, Evangelou N, Morris PG. Demonstrating the perivascular distribution of MS lesions in vivo with 7-Tesla MRI. Neurology 2008; 70: 2076–8.

Tallantyre EC, Dixon JE, Donaldson I, Owens T, Morgan PS, Morris PG, et al. Ultra-high-field imaging distinguishes MS lesions from asymptomatic white matter lesions. Neurology 2011; 76: 534–9.

Tallantyre EC, Morgan PS, Dixon JE, Al-Radaideh A, Brookes MJ, Evangelou N, et al. A comparison of 3T and 7T in the detection of small parenchymal veins within MS lesions. Invest Radiol 2009; 44: 491–4.

Tallantyre EC, Morgan PS, Dixon JE, Al-Radaideh A, Brookes MJ, Morris PG, et al. 3 Tesla and 7 Tesla MRI of multiple sclerosis cortical lesions. J Magn Reson Imaging 2010; 32: 971–7.

Todorich B, Pasquini JM, Garcia CI, Paez PM, Connor JR. Oligodendrocytes and myelination: the role of iron. Glia 2009; 57: 467–78.

Walton JC, Kaufmann JCE. Iron deposits and multiple sclerosis. Arch Pathol 1984; 108: 755–6.

Ward RJ, Crichton RR, Taylor DL, Della Corte L, Srai SK, Dexter DT. Iron and the immune system. J Neural Transm 2011; 118: 315–28.

Wattjes MP, Barkhof F. High field MRI in the diagnosis of multiple sclerosis: high field-high yield? Neuroradiology 2009; 51: 279–92.

Yao B, Bagnato F, Matsuura E, Merkle H, van Gelderen P, McFarland H, et al. Towards an in-vivo and post-mortem characterization of chronic multiple sclerosis lesions using susceptibility related mechanisms of contrast at ultra-high field MRI with R2* and phase images. Proc Intl Soc Mag Reson Med 2010; 18: 5124.

Yao B, Li TQ, Gelderen P, Shmueli K, de Zwart JA, Duyn JH. Susceptibility contrast in high field MRI of human brain as a function of tissue iron content. Neuroimage 2009; 44: 1259–66.